Journal of Materials Processing Technology 210 (2010) 941–950

Contents lists available at ScienceDirect

Journal of Materials Processing Technology

journal homepage: www.elsevier.com/locate/jmatprotec

3D finite element modeling of the thermally induced residual stress in the hybrid laser/arc welding of lap joint

Fanrong Kong, Radovan Kovacevic*

Research Center for Advanced Manufacturing, Southern Methodist University, 3101 Dyer Street, Dallas, 75205, TX, USA

ARTICLE INFO

Article history:
Received 3 April 2009
Received in revised form 6 August 2009
Accepted 9 February 2010

Keywords:
Laser welding
Gas tungsten arc welding (GTAW)
Hybrid laser/arc welding
Finite element model
Residual stress

ABSTRACT

In this study, a three-dimensional (3D) finite element model is developed to investigate thermally induced stress field during hybrid laser–gas tungsten arc welding (GTAW) process. In the hybrid welding case, we focus on the GTAW process sharing common molten pool with laser beam and playing an augment role in the hybrid welding system. An experiment-based thermal analysis is performed to obtain the temperature history, which then is applied to the mechanical (stress) analysis. A modified material model is used to consider the influence of face-to-face contact between the top and bottom metal sheets in the thermo-mechanical analysis of welding lap joints. Results show that the normal stress components prevail in the weld zone during hybrid welding process, and maximum thermal stress exceeding the yield point of material exists at the heat affected zone (HAZ) near the weld pool. Increasing the welding speed causes the penetration and width of weld bead to decrease, and the thermal stress concentration at the welded joint is also reduced accordingly. After welding and cooling down, longitudinal tensile stress (SZ) and transverse compressive stress (SX) are retained in the formed weld, and the higher longitudinal compressive stress exists around the weld bead. In addition, a series of experiments are performed to validate the numerical results, and a qualitative agreement is achieved. Compared to the welded joint obtained by GTAW and laser welding alone, the residual stress concentration in the weld joint obtained by hybrid laser–GTAW is the minimal one.

1. Introduction

Steen (1980) showed that an addition of electric arc to the laser beam used for welding and cutting could decrease the needed power of laser with respect to the case if only laser is used for welding. Subsequently, the laser-based hybrid welding technology development was initiated not only at the academic level but also at industrial level, which has been described in detail in the works published by Peyffarth and Krivt (2002) and Petring and Fuhrmann (2004). The advantages of the hybrid welding technique compared to pure laser welding or arc welding are well known and include an increase in (a) the welding speed, (b) the weldable material thickness, (c) the gap bridging ability, and (d) the welding process stability and efficiency. Rayes et al. (2004) analyzed experimentally on the bead geometry the influence of various hybrid welding parameters, such as the welding speed, arc current, laser power, and inclined angles of the gas tungsten arc welding (GTAW) torch and laser head. Chen et al. (2006) also experimentally studied the hybrid laser–arc welding of stainless steel and observed the interaction between the laser beam and arc plasma. The classification, characteristics, and applications of hybrid laser beam welding are further described by Mahrle and Beyer (2006). Recently, Liu et al. (2004) presented a hybrid laser–tungsten inert gas (TIG) arc welding of the AZ31B magnesium alloy. They use optical microscope (OM) and electron probe microanalysis (EPMA) techniques to investigate the weldability and microstructure of a magnesium alloy in the cases of hybrid laser–tungsten inert gas (TIG) welding, laser welding alone and TIG welding. They found that the welding speed of hybrid laser–arc welding is equal to the speed of laser beam welding, but higher than that of TIG by acquiring the same level of weld quality. In addition, in the fusion zone of hybrid laser/arc welding, equiaxed grains exist, whose sizes are smaller than that obtained from TIG welding but larger than those from laser beam welding. In monitoring of welding process, Huang et al. (2007) present an infrared temperature measurement method to eliminate the interfering radiation in the laser–TIG hybrid welding of magnesium alloys, and acquire an accurate distribution of the temperature field of the weld.

In laser welding alone and hybrid laser/arc welding of high strength aluminum alloys, a large number of transverse cracks are also found in the weld fusion zone, as reported by Hu and Richardson (2006). It is indicated that the cracking is related to the presence of the elongated isotherms along the welding direction, which induce a transverse tensile strain in the weld fusion zone during the cooling phase. An additional heat source could be added to alter the temperature distribution and to reduce the

* Corresponding author.
E-mail address: kovacevi@lyle.smu.edu (R. Kovacevic).

0924-0136/$ – see front matter © 2010 Elsevier B.V. All rights reserved.
doi:10.1016/j.jmatprotec.2010.02.006

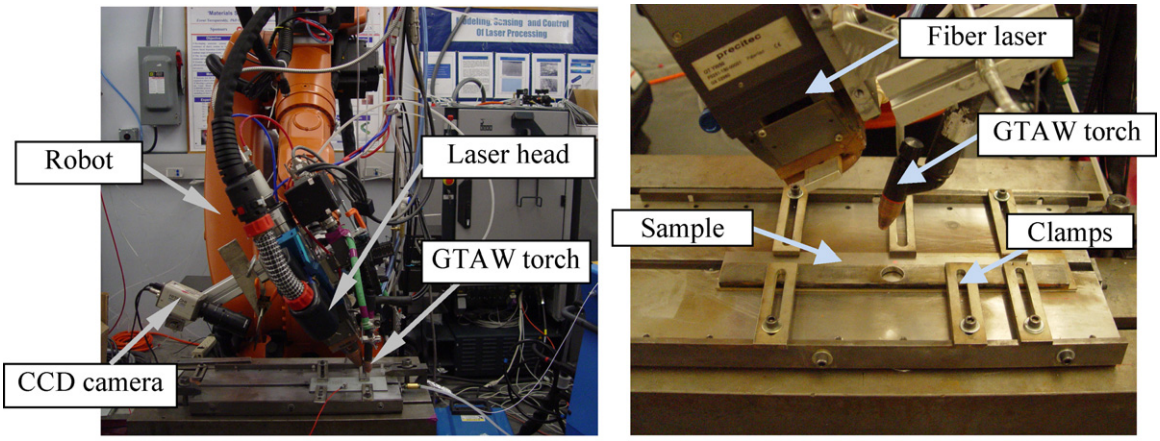

(a) Photo of experimental configuration

(b) Close-up of the laser head and arc torch

Fig. 1. Experimental setup of laser–arc hybrid welding system. (a) Photo of experimental configuration; (b) Close-up of the laser head and arc torch.

cracking tendency (Hu and Richardson, 2006). It can be seen that an inevitable presence of thermal deformation and residual stress causes potential cracking or an overlarge deformation of the welded joints. Therefore, in order to control the weld quality, it is necessary to study the influence of welding parameters on the thermal stress evolution and the sheets deformation during the welding process.

Applying the simulation method to study the thermal and mechanical processes is a cost-efficient way to understand the physical mechanisms presented in the hybrid welding process. So far, numerical and experimental investigations of welding residual stresses and controlling weld deformation focus mainly on the conventional electrical arc welding and partly on the laser welding processes. Moraitis and Labeas (2008) present a thermo-mechanical finite element model to predict the residual stress and distortion fields for laser beam welding of aluminum lap joints. In this analysis, a keyhole model is introduced to predict the keyhole size and shape required for the thermal analysis. However, the contact heat transfer between the top and bottom sheets is ignored. Abdulaliyev et al. (2007) apply a photothermoelastic model to investigate the thermal stress concentration in the butt-jointed thick plates of different materials where the residual stresses are not considered.

In modeling of hybrid laser/arc welding processes, Chen et al. (2002) tried to analyze the heat transfer mechanism in the hybrid laser–TIG welding process, and presented an energy-reduction mode point-line heat source model to simulate the heat transfer and energy interaction mechanism. However, the influence of variable location of laser and arc on energy redistribution of hybrid heat source is not considered, which directly influences the temperature distribution in the welding process according to the previous experimental measurements (Peyffarth and Krivt, 2002). Zhou and Tsai (2008) develop a mathematical model to solve the temperature distribution and fluid flow in the molten pool generated by the hybrid laser–metal inert gas (MIG) keyhole welding process, in which, a volume of fluid (VOF) method is used to track the evolution of the molten pool free surface, and the enthalpy method is employed for latent heat. In addition, Ribic et al. (2008) develop a three-dimensional (3D) heat transfer and fluid flow model to study the GTA/laser hybrid welding process, as well as the GTAW and laser welding only. However, to the best of our knowledge, there are no detailed numerical studies on the thermal stress evolution and residual stress distribution in the hybrid laser/arc welding so far. In the proposed study, a numerical model of thermo-mechanical analysis is developed to simulate the temperature distribution and thermal stress evolution during the hybrid laser/arc welding process. To verify the numerical model, a series of experiments are performed.

2. Experiment procedure

Fig. 1 shows the experimental setup of the hybrid laser–GTAW welding system, and a lap joint configuration is chosen. The system comprises a fiber laser with power of 4 kW and a GTAW power source with arc current up to 250 A. The laser welding head with the GTAW torch is attached to a six-axis high precision robot. Main welding parameters are listed in Table 1. In this study, the arc torch shares common weld pool with a laser beam. It is assumed that forced convection is present at the bottom surface of the coupon due to the flow of inert gas. Argon with a flow rate of 30 SCFH is used as the inert gas. Additionally, the coupon is in contact with the fixture and some heat losses occur through the conduction between the coupon and the fixture. The geometrical size of each coupon is 50 mm in length, 20 mm in width, and 1.4 mm in thickness (see Fig. 2a). The lap length is set at 25 mm. In this study, four cases of hybrid laser–GTAW experiment with different welding speeds of 20 mm/s, 25 mm/s, 30 mm/s, and 40 mm/s are performed to validate the thermo-mechanical finite element model. At the same time, two-level laser powers at 2.5 kW and 3 kW are used, and the two-level arc current of GTAW are set at 120 A and 160 A; and voltage are set at 17.0 V and 15.1 V, respectively. As comparisons, laser welding only and GTAW are performed separately as well.

Once the welded specimen is acquired, a part of it is cut for residual stress testing, and the remaining part is used for the metallurgical measurement of the cross-sections of the weld bead. A water jet machine is used to cut the coupon for testing, and the coupon size is same with the geometry in the modeling. An X-ray diffraction machine is used to measure the residual stress distribution at the weld surface across the weld bead, and a measured path is shown in Fig. 2b.

Table 1
Main welding parameters used in this study.

Welding speed, v	20–40 mm/s
Electrode angle, θ	14°
GTAW current, I	120–160 A
Arc column diameter, $2R_a$	6 mm
Laser power, P_{laser}	Max. 4 kW
Laser beam angle, Φ	11°
Laser focal spot diameter, $2R_l$	0.6 mm

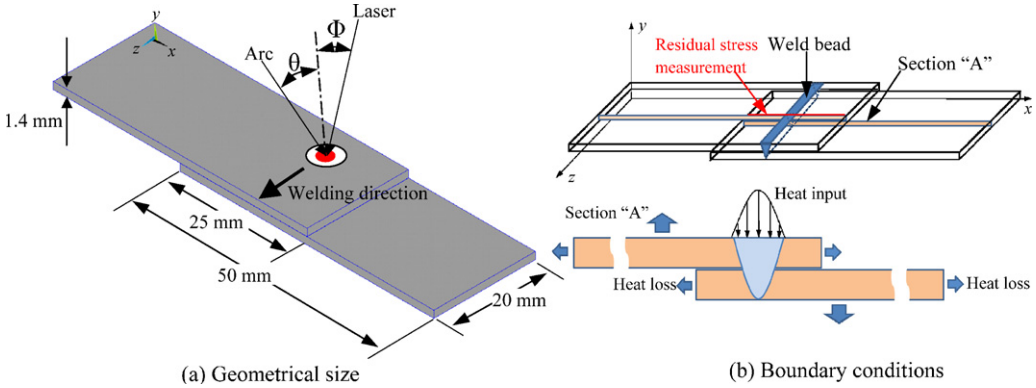

Fig. 2. Geometry and boundary conditions of lap joint.

3. Finite element modeling

3.1. Temperature field solution

The governing equation used to analyze the temperature field can be specialized to a differential control volume and shown as follows:

$$\rho c\left(\frac{\partial T}{\partial t}+\{V\}^T\{L\}T\right)+\{L\}^T\{q\}=\dot{q}_{\text{laser}}(x,y,z,t) \tag{1}$$

where ρ is the density, c is the specific heat, and T is the location-time dependent temperature. $\{L\}$ is the vector operator, $\{L\}=\begin{Bmatrix}\frac{\partial}{\partial x}\\ \frac{\partial}{\partial y}\\ \frac{\partial}{\partial z}\end{Bmatrix}$; $\{V\}$ is the velocity vector for mass transport of heat, $\{V\}=\begin{Bmatrix}v_x\\ v_y\\ v_z\end{Bmatrix}$. $\dot{q}_{\text{laser}}(x,y,z,t)$ is the heat generation rate per unit volume, that results from the laser-radiation induced volume heat input and given by (Kong et al., 2008):

$$q_{\text{laser}}(x,y,z,t)=\eta_l\frac{P_{\text{laser}}\cos\phi}{2\pi R_l^2}\times\exp\left(-\frac{(x-x_0)^2+[z+(L-y)\tan\phi-vt-h]^2\cos^2\phi}{2R_l^2}\right)\cdot\left(\frac{y}{L^2}\right)\cdot\delta_1(x,y,z,t) \tag{2}$$

where η_l is the efficiency of laser energy absorbed into material, P_{laser} is the nominal power of the laser beam, ø is the inclination angle of the laser head and ø is set at 11°, x_0 is the location of the laser head along the x-coordinate and $x_0=37.5$ mm, L is the whole thickness of the lap joint, R_l is the effective radius of the laser beam and R_l is set at 0.3 mm, h is the stand-off distance between the center of laser beam and the center of the electric arc and $h=0$ in this study. $\delta_1(x,y,z,t)$ is the location control function and shown as follows:

$$\delta_1(x,y,z,t)=\begin{cases}1, & \text{while } (x-x_0)^2+[z+(L-y)\tan\phi-vt-h]^2\cos^2\phi\le R_l^2;\\ 0, & \text{otherwise.}\end{cases} \tag{3}$$

$\{q\}$ is the heat flux vector, and Fourier's law is used to relate the heat flux vector to the thermal gradient:

$$\{q\}=-[D]\{L\}T \tag{4}$$

Where the conductivity matrix $[D]$ is given by:

$$[D]=\begin{bmatrix}K_{xx}&0&0\\0&K_{yy}&0\\0&0&K_{zz}\end{bmatrix} \tag{5}$$

K_{xx}, K_{yy}, K_{zz} are the conductivity in the element along the x, y, and z directions, respectively.

Substituting Eq. (2) into Eq. (1) and ignoring the effect of fluid flow in the weld pool on the temperature field of the welded joint, i.e. letting $\{V\}=0$, the governing equation of temperature field solution can be further shown below:

$$\rho c\left(\frac{\partial T}{\partial t}\right)=\{L\}^T([D]\{L\}T)+\dot{q}_{\text{laser}}(x,y,z,t) \tag{6}$$

In addition, the boundary conditions are considered.

(1) Specified heat flow input acting over the weld bead surface S_1:

$$\{q\}^T\{\beta\}=-q* \tag{7}$$

where $\{\beta\}$ is the unit outward normal vector; q^* is the input heat flow that results from the arc heat source and given by $q*=q_{\text{arc}}(x,y,z,t)\cdot\delta_2(x,y,z)$. S_1 denotes the surface area of the lap joint under arc heating. The whole schematic view of the hybrid heat sources in the welding system is shown in Fig. 2(a), and the boundary conditions are indicated in Fig. 2(b).

Here, the surface heat source model for the arc can be given by (Kong et al., 2008):

$$q_{\text{arc}}(x,y,z,t)=\eta_a\frac{P_{\text{arc}}\cos\theta}{\pi R_a^2}\exp\left(-\frac{(x-x_0)^2+(z-vt)^2\cos^2\theta}{2R_a^2}\right) \tag{8}$$

where η_a is the efficiency of arc energy absorption into the material, θ is the inclined angle of the arc torch, P_{arc} is the nominal power of the arc, R_a is the effective radius of the arc column and R_a is set at 3 mm.

The location-controlled function $\delta(x,y,z)$ is specified as:

$$\delta_2(x,y,z)=\begin{cases}1, & \text{while } y=L;\\ 0, & \text{otherwise.}\end{cases} \tag{9}$$

(2) Specified convection and radiation heat loss acting over surface S_2 (Newton's law of cooling) is given as:

$$\{q\}^T\{\beta\}=h_f(T_S-T_\infty)+\sigma\Im(T_S^4-T_\infty^4) \tag{10}$$

where h_f is the heat convection coefficient acting on the surfaces of the welded joint, T_∞ is the bulk temperature of the surrounding air, T_S is the surface temperature, σ is Stefan–Boltzmann constant, and $\Im$ denotes the effective emissivity due to radiation heat sink. S_2 denotes the surface area of lap joint exposure to the environment.

Combining Eq. (4) with Eqs. (7) and (10), and integrating them over the volume of the element, the governing equation of temper-

ature field solution used in this study is given below:

$$\int_{\text{vol}} \left(\rho c \left(\frac{\partial T}{\partial t} \right) \delta T + \{L\}^T ([D]\{L\}) T \right) d(\text{vol}) = \int_{S_1} \delta T q \times dS_1 - \int_{S_2} \{\delta T h_f (T - T_\infty) + \delta T \sigma \Im (T^4 - T_\infty^4)\} dS_2 + \int_{\text{vol}} \delta T \dot{q}_{\text{laser}}(x, y, z, t) d(\text{vol}) \quad (11)$$

where vol denotes the volume of the element, and δT denotes an allowable virtual temperature dependent on the location x, y, z, and time t.

3.2. Stress–strain relationships

The following thermal elastic-plastic constitutive equations are used in the mechanical (stress) simulation (ANSYS Inc, 2007):

$$[d\sigma] = [D^{ep}][d\varepsilon] - [D^{th}]dT \quad (12)$$

and

$$[D^{ep}] = [D^e] + [D^p] \quad (13)$$

where $d\sigma$ denotes the stress increment, $d\varepsilon$ denotes the strain increment and dT denotes the temperature increment, $[D^e]$ denotes the elastic stiffness matrix, $[D^p]$ denotes the plastic stiffness matrix, and $[D^{th}]$ denotes the thermal stiffness matrix.

The boundary conditions in the mechanical analysis are taken in consideration that one edge of the lap joint is fixed, i.e. ($Ux = Uy = Uz = 0$), and the other one is only transversely shrinkage free, i.e. ($Uy = Uz = 0$).

3.3. Implementation of finite element analysis

3.3.1. Material parameters definition

A gap with variable size usually exists in the lap joint configuration of industrial operations. Therefore, a gap-free configuration could be thought of as a special case of gap value approaching zero, which is chosen in this study to investigate the thermal distribution of the hybrid laser/arc welding process. The contact heat transfer that exists between the top sheet and bottom sheet before they are welded is generally ignored in the theoretical and numerical thermal analysis in previous work (Abdulaliyev et al., 2007). Recently, some reports experimentally show that the reduction in the weld distortion and the level of residual stresses of joint could be achieved by controlling the gap thickness (Peyffarth and Krivt, 2002). In order to further study the thermal and mechanical behaviors of the welded material in the hybrid laser and arc welding technique, we define the air film-AISI 1018 steel hybrid material model with an ignorable gap size between two sheets in order to handle the face-to-face contact heat transfer. It is assumed that the thermo-physical properties of the gap belong to air film when the temperature of the gap location combined with the top steel sheet is lower than the melting point of steel, and they belong to AISI 1018 steel when the temperature of the gap reaches or exceeds the melting point of steel. In addition, the stress value at the weld pool region should decrease to zero. So, a revised mechanical property model is introduced in the following section in order to involve the molten pool region into the thermal stress computation process. The main idea is that the elastic modulus of sheet material at a temperature higher than the melting point of steel is set to an exceedingly low value instead of zero. The real reason for this adjustment is to reasonably reduce the

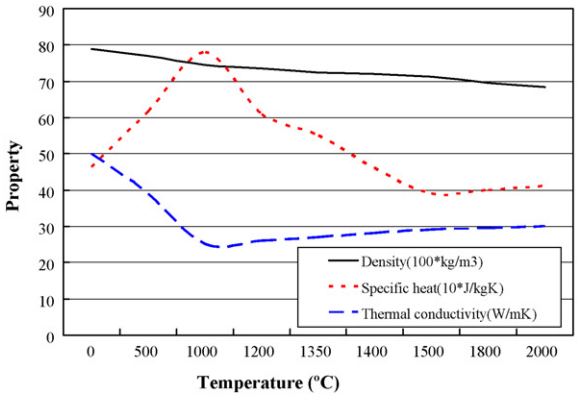

(a) AISI 1018 steel - thermal property

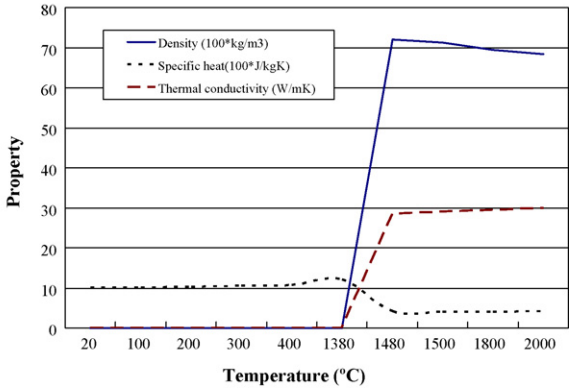

(b) Contact model at the interface of sheets

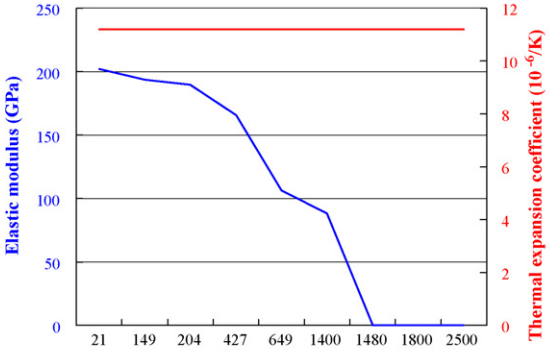

(c) AISI 1018 steel-mechanical property

Fig. 3. Material parameters used in this study. (a) AISI 1018 steel-thermal property, (b) contact model at the interface of sheets, and (c) AISI 1018 steel-mechanical property.

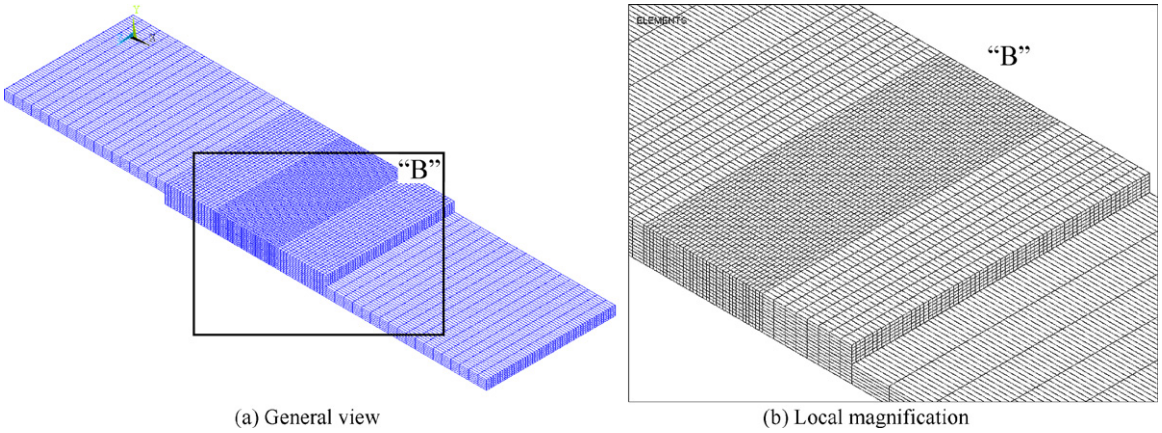

Fig. 4. Finite element mesh used in thermo-mechanical analysis. (a) General view; (b) Local magnification

computational cost and increase the convergence rate because the exceeding temperature-sensitive physical parameters obviously increase the difficulty of simulation convergence during the finite element analysis. In addition, to further simulate the residual stress of the welded joint, an elastic-plastic material model is used in the mechanical analysis module, and an isotropic hardening plasticity model is chosen to consider the plasticity in the ANSYS code (ANSYS Inc, 2007). In ANSYS 11.0, elasticity is defined by Young's modulus and Poisson's ratio, and plasticity is defined by yield stress and the elastic-plastic tangent modulus. Moreover, the von Mises stress is used to predict yielding of the welded joint. In this study, the yield stress of AISI 1018 steel is set at 350 MPa, and the elastic-plastic tangent modulus is set at 2000 MPa. The other thermal and mechanical parameters used in this study are shown in Fig. 3.

3.3.2. *Numerical implementation of thermal and mechanical analysis*

The finite element meshes used in both thermal and mechanical (stress) calculations are shown in Fig. 4. A non-uniform mesh along the welded joint is chosen. The much finer mesh is placed near and along the weld bead in order to assure enough accuracy in simulation, and the courser mesh is chosen for the areas far from the weld bead in order to reduce the computation cost.

An uncoupled thermal–mechanical finite element analysis is performed in this study. A thermal analysis is first implemented to acquire the temperature history in the welding process. Subsequently, mechanical analysis is done under the temperature loads based on the previous thermal analysis. A moving heat source due to laser radiation and arc burning is loaded into the finite element model, and all of these procedures are implemented based on ANSYS Program Designed Language (APDL).

4. Results and discussion

4.1. *Temperature field of hybrid laser–GTAW welding*

Fig. 5(a) shows the contours of temperature distribution in the hybrid laser–GTAW welding process at instant of $t = 0.4001$ s. The geometry of the weld bead increases with the arc addition in the

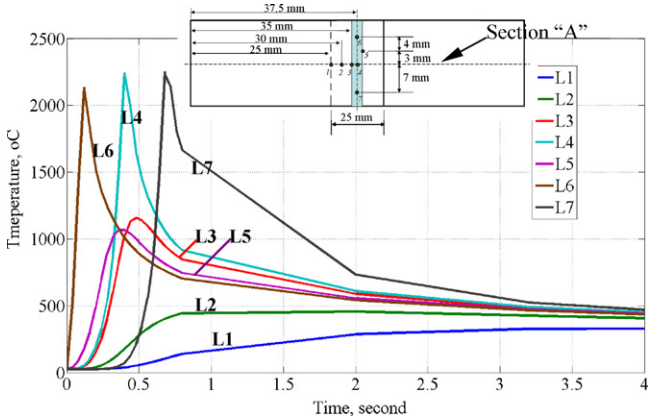

Fig. 6. Temperature evolution versus the welding time in the weld at different characteristic points by hybrid laser–GTAW welding at 25 mm/s of welding speed (laser power is 3 kW, and arc current is 120 A).

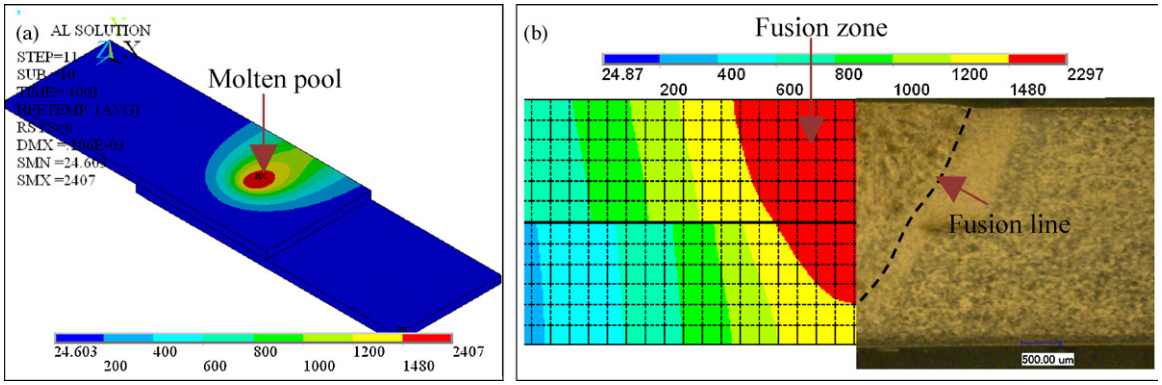

Fig. 5. (a) The modeled temperature contours at the top of the weld and (b) cross-sectional views of the modeled temperature contour versus the micrograph of the weld obtained by the hybrid laser–GTAW welding process at moment of $t = 0.4001$ s (laser power is 3 kW, and arc current is 120 A).

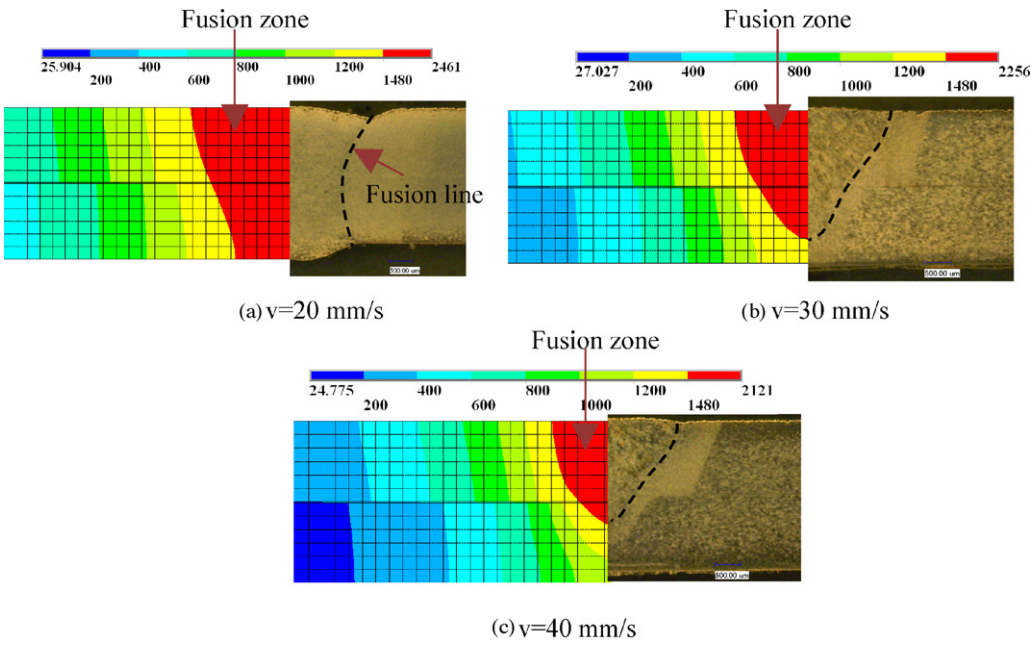

Fig. 7. Modeled temperature contours across the weld bead versus the cross-sectional micrographs of weld obtained by laser/arc hybrid welding at different welding speeds: (a) $v = 20$ mm/s, (b) $v = 30$ mm/s, and (c) $v = 40$ mm/s (laser power is 3 kW, and arc current is 160 A).

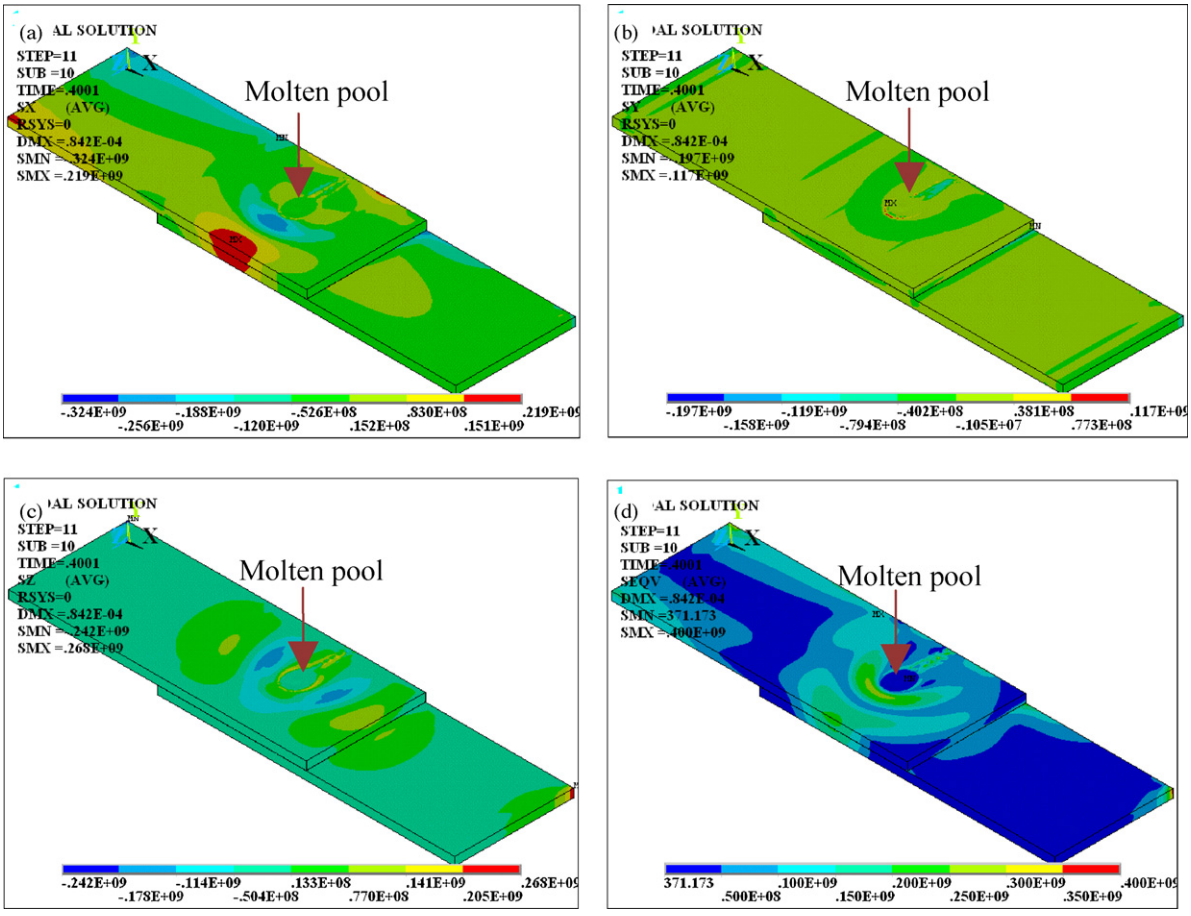

Fig. 8. 3D modeled contours of stress components in the weld obtained by hybrid laser–GTAW welding. (a) Transverse stress SX, (b) along-thickness stress SY, (c) longitudinal stress SZ and (d) von Mises equivalent stress SEQV (laser power is 3 kW, and arc current is 120 A).

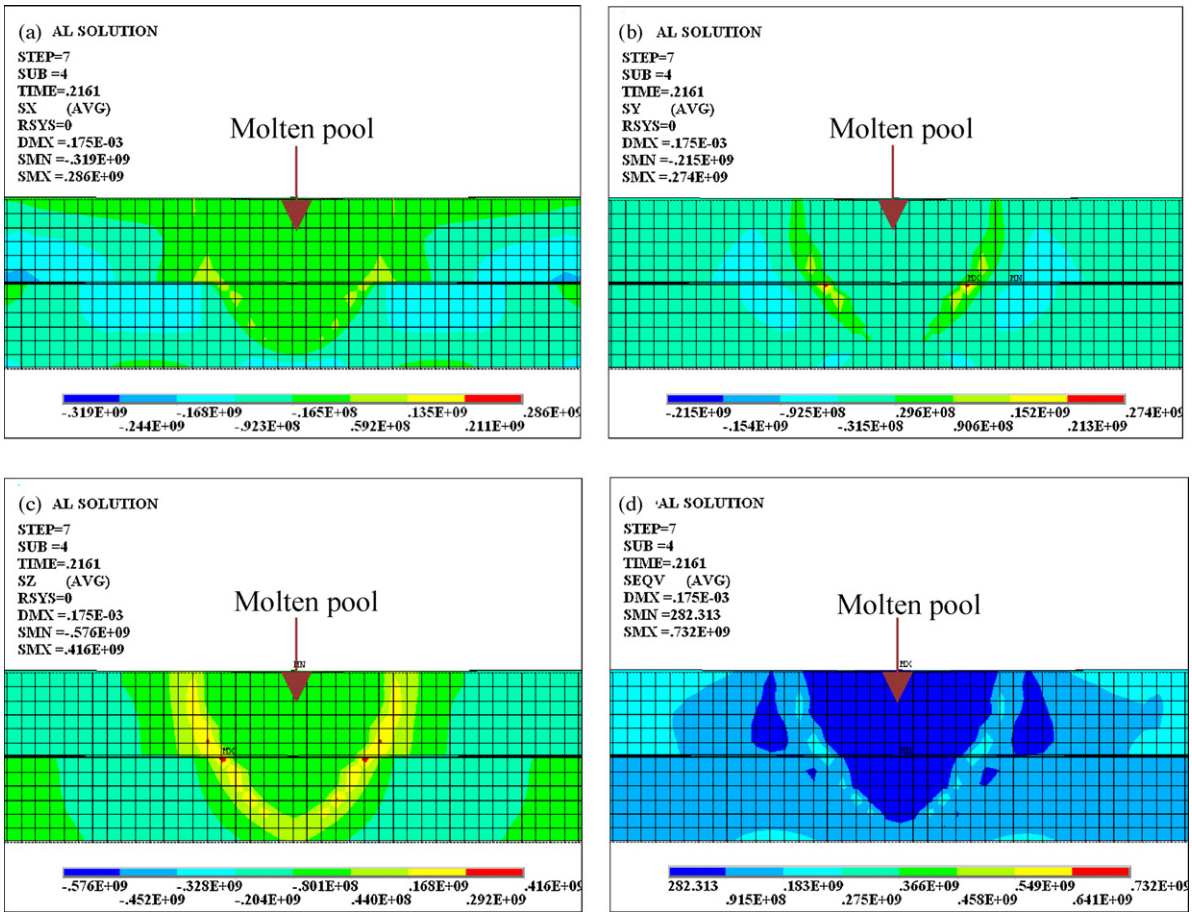

Fig. 9. Contours of thermal stress components across the cross-section of weld obtained by hybrid laser–GTAW welding. (a) Transverse stress SX, (b) along-thickness stress SY, (c) longitudinal stress SZ and (d) von Mises equivalent stress SEQV (laser power is 3 kW, and arc current is 120 A).

laser/arc hybrid weld with respect to the single laser weld bead. The more details on thermal analysis of hybrid laser–GTAW can be found in Kong et al. (2008). Fig. 5(b) indicates the comparison of halves of cross-sectional views of weld beads obtained by hybrid laser–GTAW. The left half shows the heat distribution across the weld bead obtained by the numerical simulation; and the right one is the micrograph of the cross-section of weld bead <remove-image> obtained by optical microscope. In Fig. 5b, the red region at the left modeled cross-section denotes fusion zone where temperature exceeds the melting point (1480 °C), and the dash line at the right experimental one denotes the fusion line of the weld bead. It is evident that the isotherm obtained by the finite element thermal analysis of hybrid welding process describes very well with the fusion zone and HAZ profiles of the weld. Fig. 6 shows the temperature evolution with the processing time in the weld at different characteristic points by hybrid laser–GTAW welding at 25 mm/s of

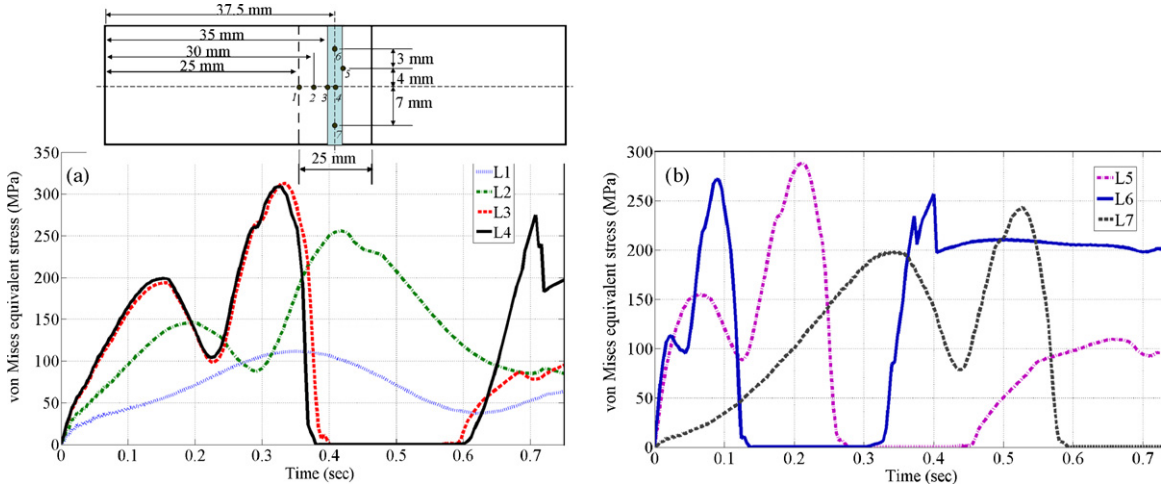

Fig. 10. Equivalent stress evolution with respect to the welding time at different characteristic points by hybrid laser–GTAW welding at 25 mm/s of welding speed (laser power is 3 kW, and arc current is 120 A).

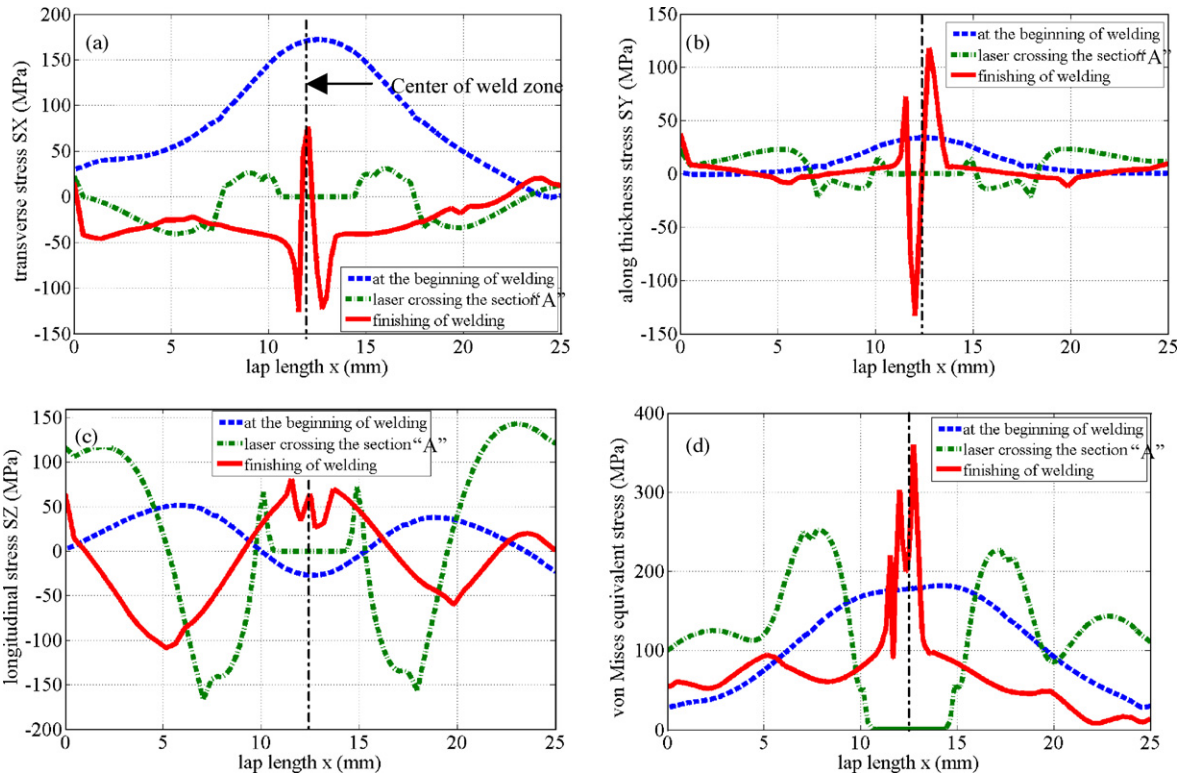

Fig. 11. Stress distribution at section A on the top of weld obtained by hybrid laser–GTAW welding. (a) Transverse stress SX, (b) along-thickness stress SY, (c) longitudinal stress SZ and (d) von Mises equivalent stress SEQV (laser power is 3 kW, and arc current is 120 A, and welding speed is 25 mm/s).

welding speed. At the locations L3, L4, L5, L6, and L7, the maximum temperature exceeds the melting point of the material of 1480 °C. The maximum temperature at the other locations shown in Fig. 6 is lower than 1480 °C, which means that all of them are outside of the fusion zone.

The influences of the welding speed on the geometry of the weld bead and temperature field are also studied based on the finite element model. Fig. 7 shows the thermal analysis results (left side) and micrographs (right side) across the cross-section of the weld bead obtained by hybrid laser–GTAW welding process. The numerical and experimental results show that penetration and width of the weld bead tend to increase with the decrease in the welding speed.

4.2. Stress field of hybrid laser–GTAW welding

The stress and strain evolutions are calculated based on the obtained temperature field by finite element thermal analysis. Fig. 8(a)–(c) shows the contours of the normal stress components, and the equivalent stress shown in Fig. 8(d). It is clearly indicated that the higher stress concentration exists at the HAZ around the molten pool, and the proposed mechanical analysis also deals with the assumption that there is a small level of stress in the weld pool. Fig. 9 shows the cross-sectional view of stress distribution at the weld pool region in the hybrid laser–GTAW welding. Fig. 10a and b indicates the stress evolution versus the time at several featured locations shown in top-left corner. The stress concentration in the hybrid weld decreases because of the changes of the temperature distribution caused by an arc addition. Previous numerical and experimental studies on the laser welding or arc welding show that a reasonable preheating or post-weld heat treatment could effectively reduce the residual stresses in the weld (Hu and Richardson, 2006). The performed study gives a strong implication that in the hybrid welding technique, the stress state is sensitively dependent on the welding conditions (such as arc current, welding speed, laser power, and stand-off distance between the laser and arc).

Numerical calculations have pointed out that a higher stress concentration exists at the HAZ of the lap joint obtained by the hybrid laser–GTAW welding. Moreover, stress state has an abrupt transition from tensile stress to compressive stress at the HAZ outward from the weld pool. To clearly describe the stress distribution in the lap joint, a cross-section A in the middle of the length of

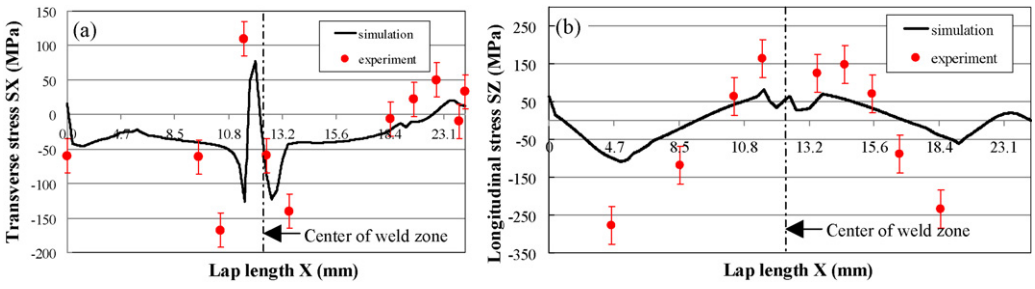

Fig. 12. Comparison of experimentally measured residual stress distribution and numerical results at section A on the top of weld obtained by hybrid laser–GTAW welding. (a) Transverse stress SX and (b) longitudinal stress SZ (laser power is 3 kW, and arc current is 120 A, and welding speed is 25 mm/s).

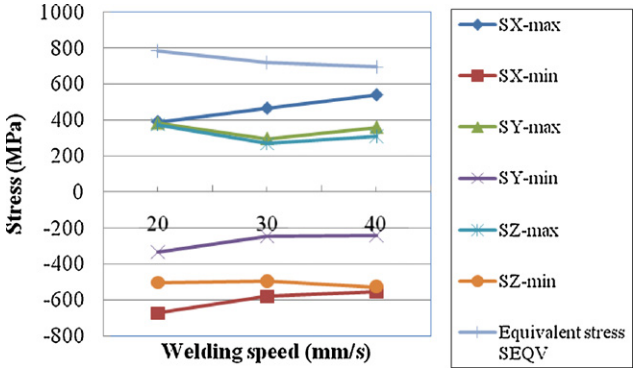

Fig. 13. Peak values of normal stress components and equivalent stress versus welding speed (laser power is set at 3 kW and arc current is set at 120 A).

the weld is chosen as the specific location (see Fig. 2b) to display the stress evolution in this study, and three typical instances are specified to determine the stress distribution: (a) at the beginning of welding (t = 0.1041 s), (b) when laser crossing the specified cross-section A (t = 0.4401 s), and (c) at the end of the welding process(t = 0.7121 s). Fig. 11 shows the stress distribution along the length of weld on the top surface at section A. Longitudinal stress component, SZ, is the highest of the three normal ones. Normal stress components prevail in the weld, and the along-thickness stress SY is relatively lower than the longitudinal stress SZ and transverse stress SX. In this case, the maximum equivalent stress is around 350 MPa, which indicates that the degree of thermal stress concentration is not too high. This result is obviously advantageous in acquiring a welded joint of higher mechanical properties.

In the hybrid welding process, as well as for any fusion welding processes, the maximum transverse tensile stress SX exists in the formed weld, and HAZ of the as-welded joint is exposed to the maximum compressive stress instead of tensile stress. To further validate the proposed thermo-mechanical model, an X-ray diffraction test machine is used to measure the residual stresses in the laser hybrid weld, and the results are shown in the Fig. 12. It can be seen that there exists a qualitative agreement of residual stress distribution between the simulation results and measured ones. However, a discrepancy existing between the numerical prediction and experimental data lies mainly on two factors. One is because of the measuring errors from the X-ray diffraction technology; the other one is because of an isotropic hardening plasticity model used in this study to consider the plastic mechanic behavior of welded material, which actually has a little difference with the true stress–strain curve of the material.

Welding speed, laser power, arc current and voltage are the main parameters influencing welding quality. Fig. 13 shows the maximum positive values (maximum tensile stresses, such as SX-max, SY-max, and SZ-max) and minimum negative ones (maximum compressive stress, such as SX-min, SY-min, and SZ-min) of thermal stress components and equivalent stress SEQV in the welded joint at three different welding speeds of 20, 30, and 40 mm/s, respectively. In general, the higher stress concentrations exist at the HAZ due to the equilibrium between the shrinkage of the weld bead caused by solidification of the molten pool and the base metal resistance to distortion. The maximum stress usually locates at both ends of the weld bead (see Fig. 8). Essentially, the welding speed increase causes the energy input into the unit volume of the weld bead at the unit time interval to decrease, and the weld pool size is reduced accordingly. The numerical results show that the maxi-

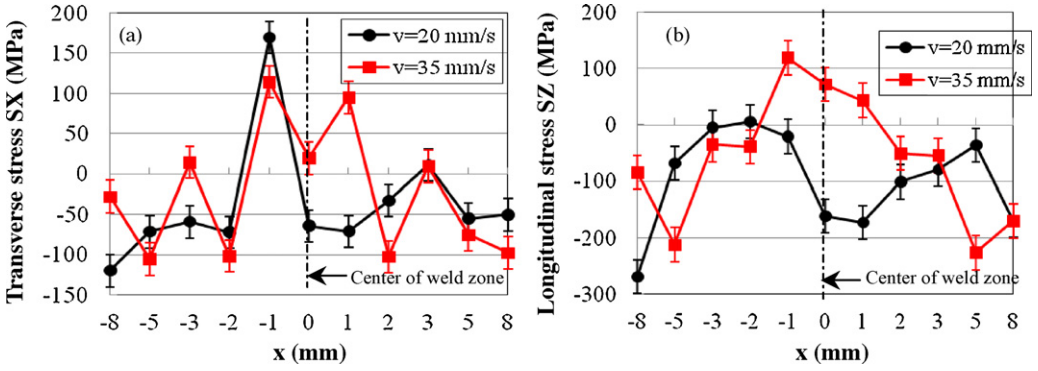

Fig. 14. Measured residual stress at the top surface across the weld bead versus welding speed. (a) Transverse stress SX and (b) longitudinal stress SZ (laser power is 3 kW, and arc current is 120 A).

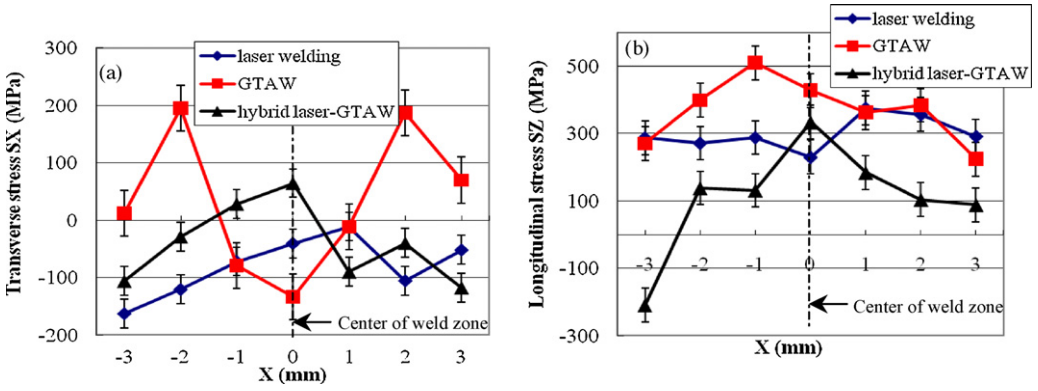

Fig. 15. Measured residual stress at the top surface across the weld beads obtained by different welding processes. (a) Transverse stress SX, (b) longitudinal stress SZ (welding speed is 15 mm/s, laser power is 2.5 kW, and arc current is 150 A).

mum normal stress components are located at the HAZ and the peak value of each one increase with the decrease in welding speed.

Fig. 14 shows the residual stress measurement results at top of the weld along the *x* direction obtained by the X-ray diffraction technique. Obviously, with an increase in welding speed, the longitudinal stress at the center of the weld bead changes from the compressive state to the tensile one. The maximum stress also reduces slightly with the increase of the welding speed. At the same time, the residual stresses at the weld zone obtained by laser welding alone and by GTAW at the constant welding speed are also measured for comparison. The laser power is set at 2.5 kW, the arc current is set at 150 A, and the arc voltage is set at 15.1 V. The residual stress measurement results clearly show that stress components (the transverse stress, SX in Fig. 15a, and the longitudinal stress, SZ in Fig. 15b) in the weld zone using only arc welding are of the highest intensities. However, the residual stress level at the weld zone obtained by hybrid laser/arc welding is of the lowest intensity, even lower than ones obtained by only laser weld as shown in Fig. 15. These results strongly support the conclusions derived from the numerical modeling results, which further validates the accuracy of the proposed thermo-mechanical finite element analysis.

5. Conclusions

A 3D thermal–mechanical finite element model is developed to investigate the temperature field and transient thermal stress field in the hybrid laser–GTAW welding for a lap joint configuration. Several conclusions can be drawn from the proposed study and shown as follows:

(1) An air-steel film model is used to consider the contact heat transfer at the interface between the top and bottom metal sheets, which is validated as an efficient way experimentally.
(2) The numerical results show that a higher stress convergence exists at the HAZ of weld, and longitudinal stress (SZ) and transverse stress (SX) prevail in the hybrid welding process. The X-ray diffraction test machine is used to measure the residual stress distribution in the welds obtained by the laser hybrid technique. A qualitative agreement exists between the numerical prediction and experimental measurement.
(3) The level of residual stress concentration in the welded joint obtained by hybrid laser–GTAW is lower than ones present in the weld joints obtained by either laser welding alone or GTAW.
(4) The proposed study could be used to better clarify the distribution of the thermally induced residual stresses during the different types of welding processes.

Acknowledgement

The authors want to thank Dr. Dechao Lin, a research engineer in Research Center for Advanced Manufacturing, for his help in the execution of experiments. This work was financially supported by NSF's Grant No. EEC-0541952.

References

Abdulaliyev, Z., Ataoglu, S., Guney, D., 2007. Thermal stresses in butt-jointed thick plates from different materials. Welding Journal 86, 201–204.
ANSYS Inc, 2007. ANSYS 11.0 Manual.
Chen, Y.B., Li, L.Q., Fang, J.F., Feng, X.S., Wu, L., 2002. Temperature field simulation of laser–TIG hybrid welding. China Welding 11 (2), 62–66.
Chen, Y.B., Lei, Z.L., Li, L.Q., Wu, L., 2006. Experimental study on welding characteristics of CO_2 laser TIG hybrid welding process. Science and Technology of Welding & Joining 11 (4), 403–411.
Hu, B., Richardson, I.M., 2006. Mechanism and possible solution for transverse solidification cracking in laser welding of high strength aluminum alloys. Materials Science and Engineering A 429, 287–294.
Huang, R.S., Liu, L.M., Song, G., 2007. Infrared temperature measurement and interference analysis of magnesium alloys in hybrid laser–TIG welding process. Materials Science and Engineering A 447, 239–243.
Kong, F., Lin, D., Yang, S., Kovacevic, R., 2008. Numerical analysis of a hybrid laser–arc welding process by using 3D nonlinear finite element model. In: The Proceeding of 47th Conference of Metallurgical (COM2008), Winnipeg, Manitoba, Canada.
Liu, L.M., Wang, J.F., Song, G., 2004. Hybrid laser–TIG welding laser beam welding and gas tungsten arc welding of AZ31B magnesium alloy. Materials Science and Engineering A 381, 129–133.
Mahrle, A., Beyer, E., 2006. Hybrid laser beam welding—classification, characteristics, and applications. Journal of Laser Application 18, 169–180.
Moraitis, G.A, Labeas, G.N., 2008. Residual stress and distortion calculation of laser beam welding for aluminum lap joints. Journal of Material Processing Technology 198, 260–269.
Petring, D., Fuhrmann, C., 2004. Recent progress and innovative solutions for laser–arc hybrid welding. In: Brandt, M., Harvey, E. (Eds.), Proceedings of the 1st Pacific International Conference on Application of Lasers and Optics.
Rayes, M., El, Walz, C., Sepold, G., 2004. The influence of various hybrid welding parameters on bead geometry. Welding Journal 83, 147–153.
Ribic, B., Rai, R., Debroy, T., 2008. Numerical simulation of heat transfer and fluid flow in GTA/laser hybrid welding. Science and Technology of Welding and Joining 13 (8), 683–693.
Steen, W.M., 1980. Arc augmented laser processing of materials. Journal of Applied Physics 51 (11), 5636–5641.
Peyffarth, P., Krivt, I.V., 2002. Welding and Allied Processes Volume I. Laser–Arc Processes and Their Application in Welding and Material Treatment. Tailor & Francis, London.
Zhou, J., Tsai, H.L., 2008. Modeling of transport phenomena in hybrid laser–MIG keyhole welding. International Journal of Heat and Mass Transfer 51, 4353–4366.